Tensile and Compressive Behavior of CHC-Reinforced Copper using Molecular Dynamics

Bruno Faria, Nuno Silvestre, and José N. Canongia Lopes*

Graphene has been extensively studied as nanofiller to produce ultra-strong and ductile metal nanocomposites but challenges such as poor adhesion at the metal–carbon interface have yet to be met. Carbon honeycombs (CHCs) are highly porous 3D graphene networks that possess a very large surface area-to-volume ratio, an outstanding physical absorption capacity and notable mechanical properties. Herein, these recently synthetized 3D CHCs are introduced in copper as nanofillers, and the mechanical properties of the nanocomposites, such as elastic modulus, tensile strength, failure strain, compressive strength, and critical strain, are obtained using molecular dynamics simulations. Three CHC lattice types are studied, and the metal–carbon interface is accurately modeled by using melting and recrystallization of the copper matrix around the nanofiller. Gains between 28% and 50% are obtained for the Young's modulus, while the tensile strength improved between 43% and 49%. Pullout tests reveal that the copper nanopillars that form by the filling of the honeycomb cells of CHC by copper atoms considerably increase the pullout force and are responsible for improvements in adhesion and in loading stress transfer.

B. Faria
IPC-Institute for Polymers and Composites
Department of Polymer Engineering
Campus de Azurém
University of Minho
4800-058 Guimarães, Portugal
E-mail: bruno.faria@dep.uminho.pt

N. Silvestre
IDMEC
Department of Mechanical Engineering
Instituto Superior Técnico
Universidade de Lisboa
Lisbon, Portugal

J. N. Canongia Lopes
CQE
Institute of Molecular Sciences
Instituto Superior Técnico
Universidade de Lisboa
Lisbon, Portugal

1. Introduction

The development of highly tough and ductile metal composites is of particular importance for structural applications, namely in transport industries. There has been ongoing research efforts to harness graphene's outstanding mechanical properties by using it as nanofiller in the mechanical reinforcement of metal nanocomposites,[1–3] thus overcoming the typical strength–ductility trade-off. However, graphene's 2D structure brings several processing limitations, such as its tendency to restack and aggregate due to strong van der Waals interactions between layers[4] or low bending rigidity that leads to surface wrinkling, thus delaying a good stress distribution of stresses.[5] One strategy to overcome these limitations is to assemble graphene in 3D networks.[6]

Carbon honeycombs (CHC) are novel carbon allotropes that consist in 3D cellular arrangements of graphene nanoribbons connected by sp^3-hybridized carbon-edge atoms. These graphene nanoribbons form the "walls" of periodic hexagonal cells in a 3D structure that resembles a honeycomb. CHCs were first theorized by Karfunkel and Dressler in 1992,[7] but only in 2016 were they experimentally synthetized by Krainyukova et al.[8] from the deposition of vacuum-sublimated graphite.

CHC's unique properties, such as high sorption and storage capacities,[9–12] membrane sieving,[13] high thermal conductivity,[14–17] or superior mechanical energy absorbing capacity[18]), have been predicted mostly by first principles and molecular dynamics (MD) methods. The latter methods were also used to explore in detail the mechanical properties of CHCs.

Using first principles, Pang et al.[19] demonstrated that CHCs have high tensile strength depending on cell size and show a marked anisotropic Poisson's ratio effect. They also realized that the honeycomb's stability is related to the combination of sp^2 bonding of graphene nanoribbons with sp^3 carbon bonding in the nanoribbons' junctions.

Zhang et al.[20] used density-functional theory (DFT) and MD to study in-plane compressive loading of CHC and found that its mechanical properties are mainly dependent on cell size and on the density of junctions between graphene nanoribbons. They also observed a self-localized deformation behavior in CHC under compression.

Gu et al.[21] employed DFT calculations and MD to show that CHCs can have remarkable strength and ductility even for small densities (0.5 g cm^{-3}). They calculated strengths as high as

**ADVANCED
SCIENCE NEWS**

www.advancedsciencenews.com

**ADVANCED
ENGINEERING
MATERIALS**

www.aem-journal.com

70 GPa for small lattice sizes and in the cell axis direction, concluding that the mechanical properties of CHCs are highly dependent on lattice size and loading direction.

Qin et al.[22] employed MD to demonstrate that the tensile strength and fracture of CHCs are strongly anisotropic. While in the cell axis direction, tensile strength reaches 70 GPa, perpendicularly to this direction, strength drops to less than half (between 15 and 23.7 GPa). The authors also reported that in tensile loading in armchair direction, CHCs present a zero-stiffness behavior. Cao and Fan[23] investigated the in-plane uniaxial compressive responses of CHC and found that, in the armchair direction, the CHC exhibits an initial linear response in stress–strain curves, while, in zigzag direction, the response is mainly nonlinear, with abrupt stress drop characteristic of shear-type instabilities. Du et al.,[14] using MD, studied the influence of cell defects on the mechanical properties of CHC and found that, while the Young's modulus is almost independent of defect concentration, both tensile strength and fracture strain can be severely reduced by increasing cell defects. Also using MD, Zhang et al.[24] analyzed the mechanical properties of CHCs under shear loading and concluded that while junction type has a negligible effect on shear strength, the stability of junctions plays a decisive role in shear response.

Zhang et al.[25] used MD to uniaxially compress CHC and unveiled that the resulting local buckling notably improves gas transportation in these structures, thus enabling a new strategy for gas storage. Yi et al.[18] studied the energy absorption capability of CHC in all three directions and found an extremely high energy absorption capacity in in-plane direction (up to 2400 J g^{-1}), particularly when compared to other known cellular materials.

Due to its porosity, CHCs have a very low mass density. In addition to their remarkable strength and thermal conductivity, this low density makes them ideal nanofillers for ultralight and multifunctional structural materials.

In this work, CHCs are introduced in copper nanocomposites as nanofillers to mechanical reinforce the metal matrix. Using MD simulations, tensile loading and compressive loading are imposed to the Cu–CHC systems, and the mechanical properties

are obtained. To improve modeling of the metal–carbon interface, the copper matrix is melted and recrystallized around the nanofiller. Cu atoms penetrate the interior of the tubular honeycomb cells and form Cu nanopillars that enhance the adhesion between the CHC structure and copper.

It should be mentioned that the interface between copper and 2D graphenic structures usually presents low adhesion. Experimentally this challenge has been addressed by using oxidized nanofiller surfaces such as reduced graphene oxide or copper oxide or by adding a third linking component, usually a metal with affinity toward both materials such as chromium.[26,27] Both strategies present promising results. Using 3D graphenic structures, such as CHCs, can be seen as an additional strategy, which can complement the previous ones.

Metal reinforcement depends on the mechanical properties of the nanofiller; the yield of recrystallization, and the stress transfer between the two materials. Therefore, in addition to the determination of the mechanical properties of the copper nanocomposites, this work also includes 1) the assessment of Cu-recrystallization yield and its characterization; 2) testing of the mechanical properties of CHCs; and 3) the determination of the pullout behavior of CHCs from the Cu matrix.

2. Computational Models

2.1. Models of the CHCs and Cu–CHC Nanocomposites

Three different CHC structures were inserted in Cu matrices originating three distinct Cu–CHC nanocomposites. The CHCs were modeled according to zigzag lattices designated by hC28, S1, and S2. The zigzag lattice designations and unit cell structures are extensively presented and studied in the work of Hu et al.[28] They are used in the present work because they represent typical CHC structures in an ample range of lattice stability. Broadly, in the S1 lattice, graphene nanoribbons (honeycomb cell walls) are joined together by sp^2 carbon bonding. This model for CHCs (see **Figure 1**a and **2**b1,b2), in which all carbon bonding originate in sp^2-hybridized carbon atoms, was first proposed by Krainyukova et al.,[8] but later abandoned when
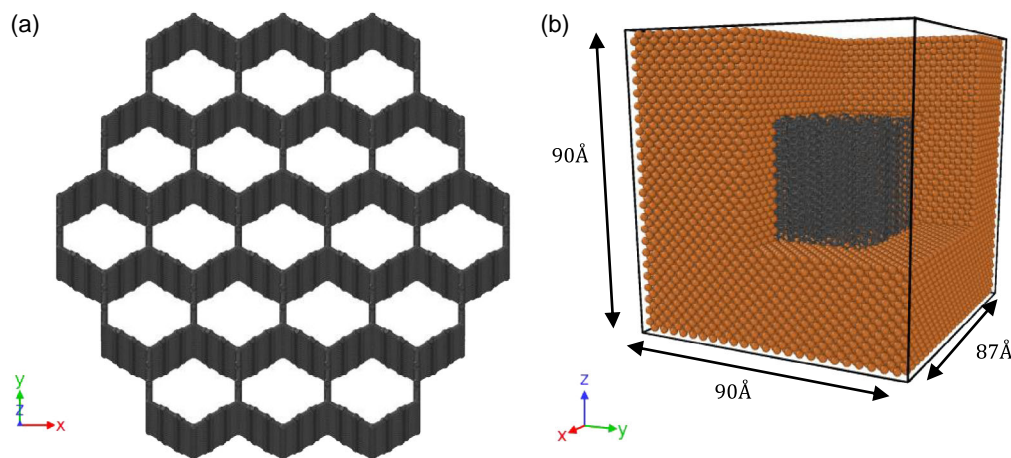

Figure 1. Different representations of the carbon honeycomb (CHC) lattices: frontal views (*yz* plane) of the a1) hC28 lattice; b1) S1 lattice; and c1) S2 lattice and zoom-in view of the CHC junctions in the a2) hC28 lattice; b2) S1 lattice; and c.2) S2 lattice.

first-principles calculations showed that graphene nanoribbon junctions are more stable with sp^3 carbon bonding.[9,19,20] The S2 lattice represents one possible stable conformation, predicted by first-principles calculations, for the structure of CHCs. In the S2 lattice, graphene nanoribbons are joined by sp^3 carbon bonding (see Figure 2c1,c2). The hC28 lattice is a theoretically more stable variation of S2, proposed by Hu et al.[28] (see Figure 1a1,a2).

The CHC structures are constructed from nineteen honeycomb cells disposed in a cylindrical shape as can be seen in Figure 1a. The dimensions and number of atoms of each CHC are showed in **Table 1**.

The single-crystal Cu matrices were modeled in the form of a square prisms, according to crystal lattice constants (*a*) and dimensions (H depth, W width, L length) and with number of atoms (*N*) given in Table 1. Notice that depth, *H*, is here defined in the [001] direction of the Cu crystal lattice. For clarification of the models see Figure 2, in which H corresponds to the *z*-direction, W to the direction, and L to the *y*-direction.

The CHCs structures were inserted in Cu matrices. First, a void was carved in the center of the Cu matrix by deleting the Cu atoms in the prescribed region and then the CHCs were positioned inside this void region, equally spaced from the Cu atoms (a minimum distance of 2 Å between the nanofillers and the metal atoms was ensured to prevent initial atomic repulsion interactions, although the following step of melting allows the reaching of an equilibrium interfacial distance between metal and nanofiller). The matrix and void dimensions and the total number of Cu atoms after the creation of void region are also presented in Table 1.

2.2. MD Simulation

The interactions between carbon atoms in CHCs were simulated by the well-known adaptive intermolecular reactive empirical bond order (AIREBO)-reactive potential.[29] In view of the objectives of this work, AIREBO was chosen as the more reasonable approach to accurately model C–C interactions, despite its well-known limitations.[30] To correct the artificially enhanced tensile force that arises when C–C bond length exceeds 1.7 Å (due to the cutoff function implementation), AIREBO is used here with the minimum C–C cutoff parameter increased to 2.0 Å.[31] Cu–Cu metallic bonding was modeled by the embedded atom model potential which has been consistently adopted to simulate metallic systems with success. The potential parameters for Cu–Cu interactions were taken from the work of Mendelev

Table 1. Data on the single-crystal copper matrix, before melting, and the carbon honeycombs structures, where *a* is the crystal lattice constant, *H* is depth, *W* is width, *L* is length (corresponding to *z*, *x*, and *y* coordinates axis) and *N* is the number of atoms of the simulation models.

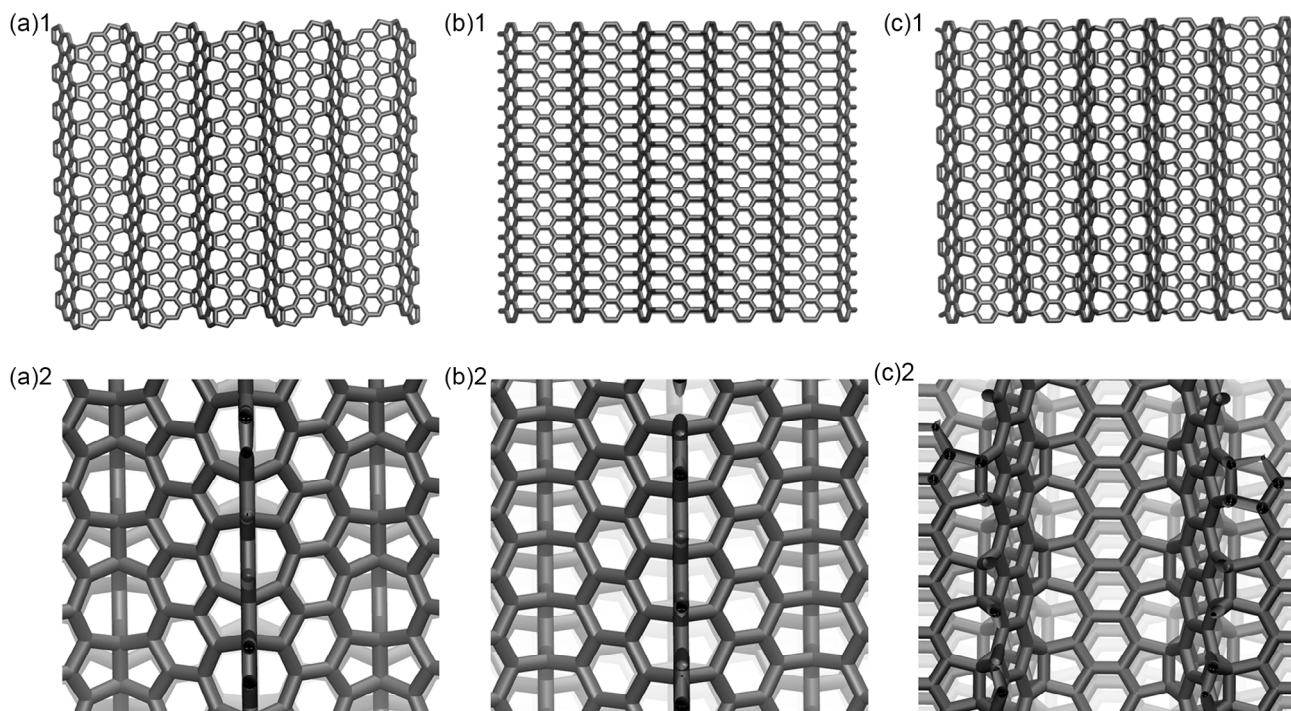| Metal	Crystal structure (space group/number)	a [Å]	H (Å)	W [Å]	L [Å]	N
Cu (before melting)	FCC ($Fm\bar{3}m$, 225)	3.615	90	90	87	46 798
Centered void space	–	–	43	57	51	–
CHC	Lattice		H [Å]	W [Å]	L [Å]	N
hC28	hC28[28]		39.1	50.2	46.4	5472
S1	S1[28]		38.9	50.6	46.7	5616
S2	S2[28]		38.9	50.5	46.6	5616

Figure 2. Schematic representations of the atomic models used to simulate a) CHCs (top view) and b) the Cu–CHC nanocomposites (the figure shows a perspective view of a Cu–CHC nanocomposite where ≈1/8 of the matrix [top section] is sliced off so that the inserted CHC can be partially seen).

ADVANCED
SCIENCE NEWS
www.advancedsciencenews.com

ADVANCED
ENGINEERING
MATERIALS
www.aem-journal.com

et al.[32] The Lennard–Jones (LJ) 12–6 potential was selected to simulate the interatomic forces between carbon atoms from CHC and Cu atoms (van der Waals forces describe these interactions).

$$E_{LJ} = 4\varepsilon \left[\left(\frac{\sigma}{r} \right)^{12} - \left(\frac{\sigma}{r} \right)^{6} \right] \quad (1)$$

where E_{LJ} is the LJ potential energy, ε is the potential well depth, σ is the van der Waals equilibrium distance of null potential, and r is the distance between atom pairs.

The respective cross-term parameters, that is, the energy minimum (well depth) ε_{a-b} and the equilibrium interatomic distance of null potential σ_{a-b} were obtained from the rules of mixture of Lorentz–Berthelot, and were given by

$$\varepsilon_{a-b} = \sqrt{\varepsilon_{a-a} \cdot \varepsilon_{b-b}} \quad (2a)$$

$$\sigma_{a-b} = \frac{\sigma_{a-a} + \sigma_{b-b}}{2} \quad (2b)$$

The calculated cross-term parameters as well as C–C (σ_{a-a} and σ_{a-a}) and Cu–Cu (ε_{b-b} and σ_{b-b}) nonbonded LJ parameters (taken from refs. [33,34]) are resumed in **Table 2**. A cutoff distance of 16.0 Å was selected for the interfacial C–Cu interactions. The MD simulations were performed using the large-scale atomic/molecular massively parallel simulator code.[35]

2.3. Melting and Recrystallization Procedure

The CHC nanofillers are composed of periodic hollow nanopillars that can potentially be filled with Cu atoms. A realistic modeling of the interface between CHC and Cu must account for this type of distribution of metal atoms to capture and measure the effect of the CHC's porosity on the mechanical properties of the nanocomposite. One method for achieving a more realistic interface is to melt the copper matrix and then recrystallize it while maintaining the nanofillers fixed (not thermostatized). This method has been previously employed by the authors for aluminum (Al) matrices and is described in detail in refs. [36,37]. A single-crystal Cu matrix and the three Cu–CHC nanocomposites (initial configurations shown in Section 2.1) were equilibrated at 2000 K and 1 atm for 300 ps within the context of an isothermal–isobaric (NPT) ensemble and using the Nosé–Hoover thermostat and barostat for temperature and pressure control. After the first equilibration step, the systems were quenched from 2000 to 10 K at a cooling rate of 0.5 K ps⁻¹. A timestep of 1 fs was used. During this melting and cooling procedure, the CHC nanofillers were kept fixed in the center of the simulation boxes. After quenching, the solidified systems were equilibrated at 10 K (NVT) for an additional 300 ps to promote system relaxation and stabilization (eliminate residual stresses). It should be noted that the aim of this cooling procedure is not the accurate determination of phase-transition temperatures for copper. Quenching methods are not reliable for that effect due to the fast cooling rates used and because nucleation and recrystallization are slow and complex processes. However, this method allows the creation of realistic interfaces with good recrystallization yields that can be directly related to the mechanical properties obtained for each nanocomposite.

2.4. Loading Procedure

After equilibration, the pure Cu and the three nanocomposites systems were subjected to compressive and tensile loading conditions to assess their mechanical behavior. The simulation boxes were deformed in the z-direction at an engineering strain rate of 1.2 ns⁻¹ (which gives approximately a velocity of 0.1 Å ps⁻¹ for tensile loading, and a velocity of −0.1 Å ps⁻¹ in the case of compression). A timestep of 2 fs was adopted for the loading tests. Globally the simulations boxes were stretched (or compressed) approximately 50 Å. The deformations were performed within the context of an NPT ensemble, employing the Nosé–Hoover thermostat and barostat to keep a temperature of 10 K and pressure of 0 atm in the non-deformed directions. Additionally, the mechanical properties of the CHCs (hC28, S1, and S2) were also independently determined. Similar to the method used for the nanocomposites, the simulation boxes were deformed in the z-direction at a velocity of 0.1 Å ps⁻¹ for tensile loading, and a velocity of −0.1 Å ps⁻¹ in the case of compression. A timestep of 1 fs was used. As performed before, the simulations were performed within the context of an NPT ensemble, employing the Nosé–Hoover thermostat and barostat to keep a temperature of 10 K and pressure of 0 atm in the non-deformed directions.

The nanocomposite systems used for the pullout process were modeled from the same recrystallized nanocomposite systems used in tensile and compressive loading but with nonperiodic boundary conditions. First, the Cu atoms inside a region delimited by $z > a$, where a is the z-coordinate of carbon atoms at the top of each CHC, were deleted (see **Figure 3**). The top of the CHC is now part of the system boundary. Then, the first layer of C atoms from the top of the CHC were fixed (not thermostatized) and then pulled from the Cu matrix at a speed of 0.05 Å ps⁻¹ until the full length of the CHCs is removed from the Cu matrix (see Figure 3). A timestep of 2 fs was employed and the simulations were performed within the context of an NVT ensemble using the Nosé–Hoover thermostat to keep a temperature of 10 K.

3. Results and Discussion

3.1. Recrystallization Yield

The melted Cu matrix completely filled the honeycomb cells of the CHC structure, hence producing a more realist interface between metal and CHC after recrystallization. Since it is known that Cu single crystals possess a face-cubic-centered (FCC) unit cell, the yield of Cu recrystallization is measured here in terms of
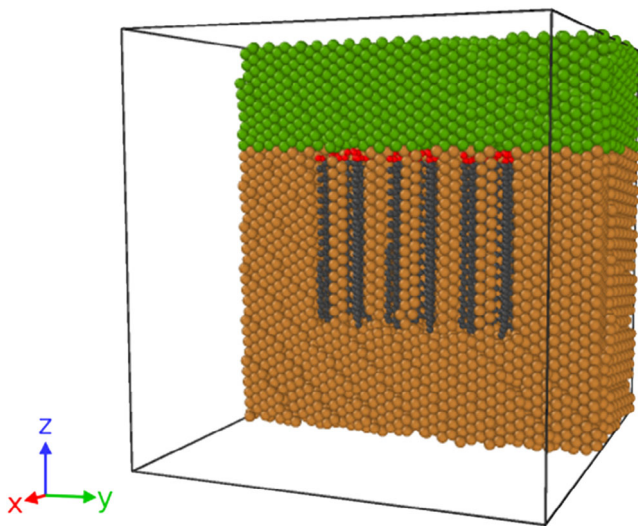
Table 2. Lennard–Jones parameters for carbon–carbon (CHC), Cu–Cu, and carbon–Cu nonbonded interactions.

Nonbonded interaction	ε_{a-b} [eV]	σ_{a-b} [Å]
C–C (CHC)[33]	0.00296	3.407
Cu–Cu[34]	0.415	2.277
C–Cu	0.0350	2.82

Figure 3. Schematic representation of the atomic model used to simulate the CHC pullout from the Cu–CHC nanocomposite. The figure shows a perspective view of a Cu–CHC nanocomposite where approximately 1/2 of the matrix is sliced off (cut for $x = 0$). Copper atoms represented in green were removed and the fixed CHC atoms are represented in red).

percentage of Cu atoms assuming an FCC structure relative to the total number of atoms. **Figure** 4b shows the evolution of the recrystallization yield of pure Cu and Cu–CHC nanocomposites with temperature. Note that although the quenching process occurred from 2000 to 10 K, Figure 4b only displays the temperature interval between 1500 and 10 K to highlight the more relevant part of the quenching curves. The pure Cu matrix reached a recrystallization yield of 94% (yellow curve). Figure 4b also shows the total number of Cu atoms assuming an FCC stabilized structure after cooling down below the threshold of 550 K (solidification temperature).

Figure 4a shows the variation of total energy with temperature. Before nucleation, the total energy curve decreases linearly with temperature during cooling. When atoms begin to organize in crystal structures (nucleation), the energy curve has a steep decline. When recrystallization ends and the Cu matrix is solidified, the total energy curve resumes the previous trend before

nucleation. The steepest slope in the total energy versus temperature curves demarks the temperature region where recrystallization occurs. Figure 4b complements Figure 4a by showing the FCC crystal growth in that temperature region. The recrystallization yield in the case of nanocomposites was inferior to that of pure Cu. For example, Cu–CHC (S1) and Cu–CHC (S2) have a recrystallization yield of 76% while the recrystallization yield of Cu–CHC (hC28) was around 72%. The inferior-recrystallization yield of the nanocomposites is due to the introduction of the CHC nanofiller into the Cu matrix which impedes a more extensive growth of the nucleated crystals. Comprehensibly 3D nanofillers seem to cause a greater disturbance in 3D crystal growth than planar nanofillers. Note that Cu atoms inside the tubular cells of the nanofiller do not have enough space to assume an FCC configuration; hence, they do not contribute for the recrystallization yield. In contrast, the solidification temperatures of the nanocomposites increase because the nanofillers facilitate nucleation. For example, for pure Cu, recrystallization occurs between 769 and 560 K, which is a much lower temperature interval than that of Cu–CHC (S1), where recrystallization occurs between 1130 and 1060 K. Similarly, the same occurs for Cu–CHC (S2), where the recrystallization temperature ranges between 1150 and 1025 K, and for Cu–CHC (hC28), where the respective interval is between 1020 and 820 K.

The solidification temperatures obtained in this work (particularly pure Cu) are clearly inferior to those predicted from experimental tests, which for Cu is approximately 1358 K. The difficulty in the prediction of phase transitions is a known issue in MD. Nucleation and crystallization processes are complex and slow and can be more accurately characterized by methods other than quenching, such as for example thermodynamic integration for determining free energy differences. The strategy presented here aims at obtaining a good distribution of metal atoms in the interface with CHC with an acceptable recrystallization yield. To this purpose, the quenching method has been shown to be adequate. Despite this, the conclusion that the presence of the 3D nanofiller facilitates nucleation, thus increasing the solidification temperature, remains valid.

Note that the algorithm used in this work to detect crystal structures is the adaptive common neighbor analysis (CNA) algorithm from Stukowski,[38] which is based on the original CNA
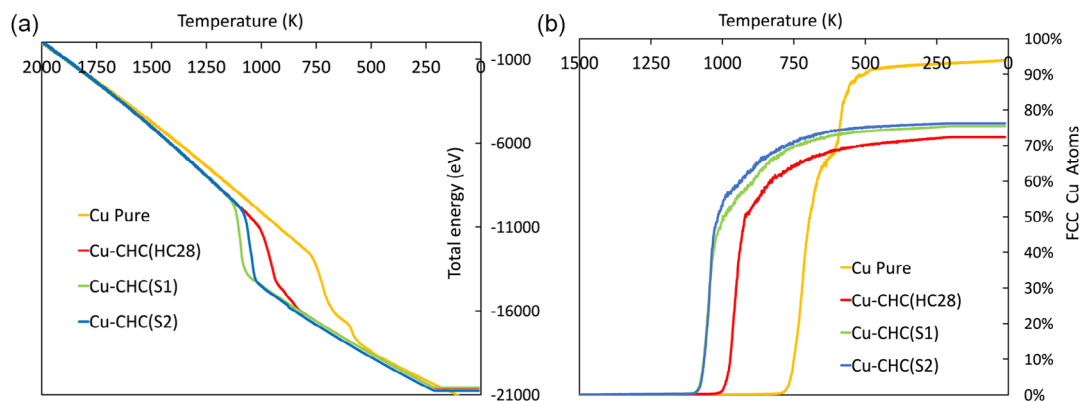

Figure 4. Variation with temperature of a) total energy and b) percentage number of Cu atoms having a face-cubic-centered (FCC) crystal structure with respect to total number of Cu atoms.

2300147 (5 of 13)

**ADVANCED
SCIENCE NEWS**

www.advancedsciencenews.com

**ADVANCED
ENGINEERING
MATERIALS**

www.aem-journal.com

algorithm from Honeycutt et al.[39] but with a variable cutoff. This algorithm is implemented in the OVITO software.[40]

Figures 5 and **6** present the recrystallized structures of pure Cu and the three Cu–CHC nanocomposites, from two different perspectives. Pure Cu has several diagonal-twining planes crossing the matrix (separating regions with different crystal orientations), some of which contain very small amorphous regions (Figure 5a,b). Despite the high-crystallization yield, the recrystallized Cu matrix is far from a single-crystal structure. In the case of Cu–CHC composites, Cu atoms have filled the hexagonal cells of CHC. Although the CNA algorithm doesn't attribute a definite structure to these "interior" Cu atoms, it can be noted that they are tightly packed and structured, forming Cu nanopillars. In the case of Cu–CHC (hC28) (Figure 5c,d), the CHC is part of a grain boundary of amorphous atoms that divide the matrix in two crystal grains. Each crystal grain is crossed by several stacking faults.

Figure 6 shows the recrystallized structures of Cu–CHC (S1) and Cu–CHC (S2). Both matrices are crossed by several twinning planes, but not by grain boundaries constituted by amorphous

atoms as was the case of Cu–CHC (hC28). The presence of the nanofiller appears to be slightly less disruptive of the crystal structure than in the case of Cu–CHC (hC28). In Figure 6b,d, it can be seen that Cu atoms are closely packed inside the CHC honeycomb cells similarly to Cu–CHC (hC28).

Differences in the structure of the nanofillers may influence the yield and the crystal defects of the recrystallization process. These differences are in the type of lattice (pore size) and in the 3D conformation of the nanofillers, which are notable in Figure 2. S1 has similar size pores, while S2 and hC28 have different size pores (regular in S2 and irregular in hC28). From Figure 6, it can be observed that pore size has little influence in crystal defect formation, since the crystal structure of Cu–CHC (S1) is very similar to that of Cu–CHC (S2). Hence, the presence of grain boundaries in Cu–CHC (hC28) can be related not to pore size or pore distribution, but to the structural irregularities in the 3D conformation of hC28 (notice the irregular "ladder" pattern at the top and bottom ends of the hC28 nanofiller in Figure 2a1).
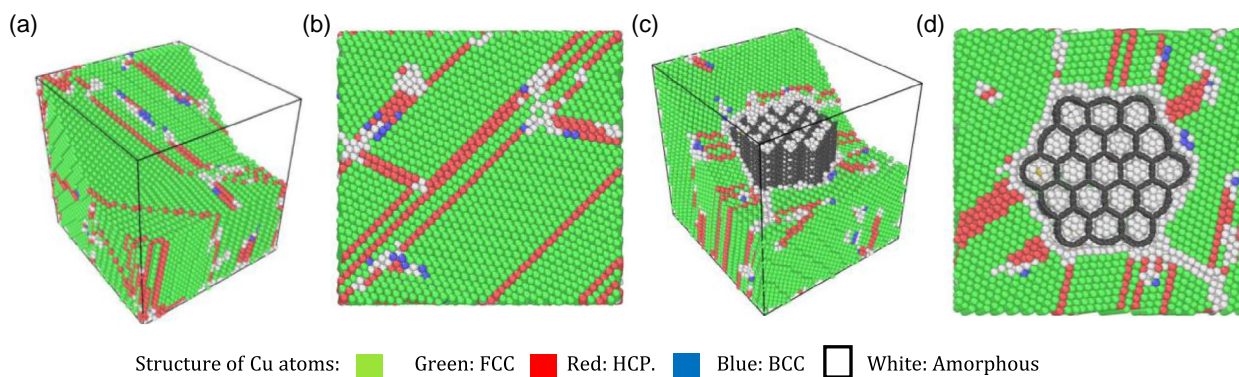

Structure of Cu atoms: ▪ Green: FCC ▪ Red: HCP. ▪ Blue: BCC ☐ White: Amorphous

Figure 5. Crystal structure of recrystallized copper matrices from two perspectives, "armchair" perspective (diagonal cut + half cut) and top-view perspective (half cut) (these perspectives try to give an in-depth account of recrystallization yield in the different matrices): a,b) are snapshots from the pure Cu matrix, while c,d) are snapshots from the Cu–CHC (hC28) matrix. Color legend: green-FCC crystal structure; red-hexagonal close-packed (HCP) crystal structure; and blue-body centred cubic (BCC) crystal structure and white-amorphous atoms.
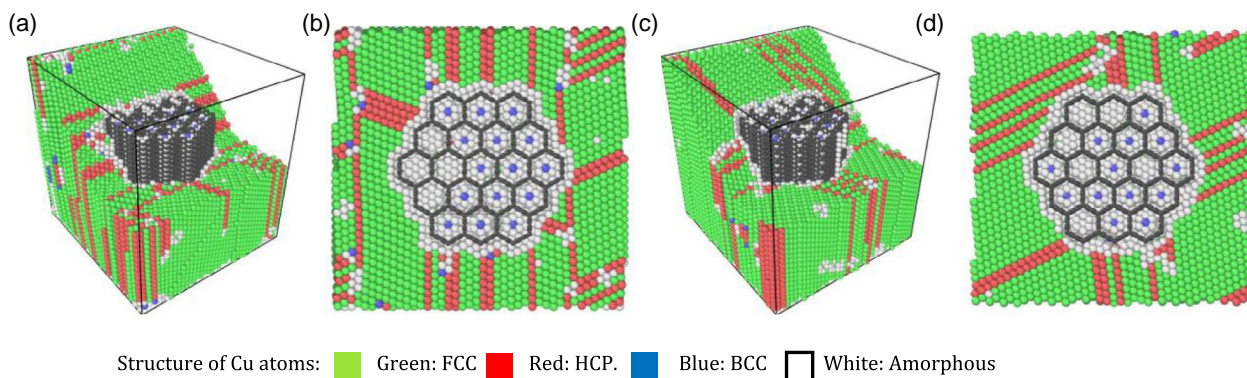

Structure of Cu atoms: ▪ Green: FCC ▪ Red: HCP. ▪ Blue: BCC ☐ White: Amorphous

Figure 6. Crystal structure of recrystallized copper matrices from two perspectives, "armchair" perspective (diagonal cut + half cut) and top-view perspective (half cut) (these perspectives try to give an in-depth account of recrystallization yield in the different matrices): a,b) are snapshots from the Cu–CHC (S1) matrix, while c,d) are snapshots from the Cu–CHC (S2) matrix. Color legend: green-FCC crystal structure; red-HCP crystal structure; and blue-BCC crystal structure and white-amorphous atoms.
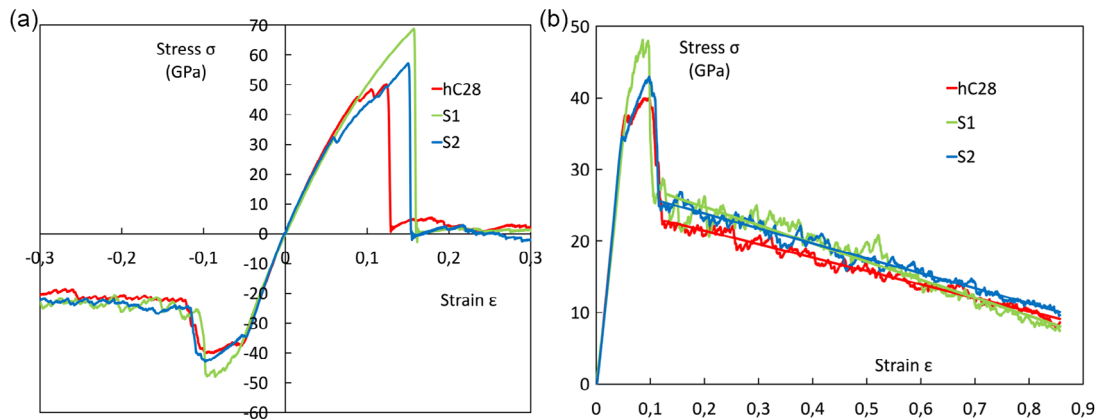
Figure 7. Stress–strain curves of the CHC structures, namely hC28, S1, and S2 when subjected to a) compressive loading ($-0.3 < \varepsilon < 0$) and tensile loading $0 < \varepsilon < 0.3$), and b) compressive loading ($0 < \varepsilon < 0.85$, stress and strain in absolute values) where trend lines are added to the stress–strain curves in the region of the post-buckling regime.

3.2. Tensile and Compressive Mechanical Properties

Essentially, the mechanical reinforcement of Cu with CHC nanofillers is strongly dependent 1) on the mechanical properties of the nanofillers and 2) on the load transfer that occurs at the interface between the two materials (adhesion). Hence, the mechanical properties of the nanofillers were tested. **Figure 7**a shows the stress–strain behavior for compressive and tensile loading of the CHCs. Tensile loading leads to a complete rupture of the CHC structure thus the stress–strain curves show a drop to approximately zero stress for rupture strain. In contrast, compressive loading leads to buckling at critical strain followed by a post-buckling behavior where the deformed structure continues to present strength. The tensile and compressive properties of the CHCs are presented in **Table 3**. The S1 conformation presents a lower Young's modulus, but higher tensile and compressive strengths, as well as higher failure strain. Note that this conformation is purely theoretical, having been put forward when no experimental data existed about CHCs. In fact, graphene nanoribbon junctions in S1 were assumed to be made by sp^2 carbon bonds; hence, the regular lattice of S1. Later it was discovered that the nanoribbons junctions are made by sp^3 carbon bonding, thus originating conformations such as hC28 and S2. The latter conformations have higher Young's modulus, but lower tensile and compressive strengths as well as lower failure strains. It can be concluded that sp^3 carbon bonding at nanoribbons junctions (apart from increasing conformation stability) originate a slightly

higher Young's modulus, albeit reducing the tensile and compressive strengths and failure strains.

In contrast, it can also be said that this type of carbon bonding at the junctions slightly increases the critical strains. The irregular patterning in pore size distribution in hC28 has a detrimental effect in most properties when compared to S2 (-12% in tensile strength, -7% in compressive strength, -17% in failure strength, -7% in critical strain, but $+2\%$ in the Young's modulus).

Most studies using MD to calculate the mechanical properties of CHC are focused on tensile and compressive loading along the armchair and zigzag direction in the xy plane.[20,22,23,25] Nonetheless, the mechanical properties for CHCs obtained here compare fairly well with the mechanical properties for tensile and compressive loading in the z-direction from other computational works[18,19,21,41–44] (see Table S1 from Section SI.2, Supporting Information). Using DFT, the values for Y obtained for the hC28, S1, and S2 structures show deviations of less than 12% in comparison to the values obtained in the present work.[26] MD studies on the tensile properties of S1 and S2 structures using the same potential and also at 10 K show slightly higher deviations (between -7% and -16% for ref. [42] and -23% for ref. [39]); however, these deviations may have to do with the method used for calculating Y. In this work, the Y was obtained in the elastic region that includes compressive and tensile loading, not only tensile loading as is the case for the mentioned references.

Figure 7b shows the compressive stress–strain curve in a wider strain range ($0 < \varepsilon < 0.85$), as the behavior after the peak stress (post-buckling behavior) is particularly relevant. In this case, it is very interesting that the three CHCs show a similar trend: for increasing compressive strains ($\varepsilon > 0.12$), the stresses decrease at a fairly slow rate and do not drop to zero. The three linear trend lines have the following equations

$$\sigma_{hC28} = 25,19 - 18,77\varepsilon \tag{3a}$$

$$\sigma_{S1} = 29,81 - 25,35\varepsilon \tag{3b}$$

$$\sigma_{S2} = 28,03 - 20,91\varepsilon \tag{3c}$$

Table 3. Young's moduli, Y in GPa, are Y values from ref. [28], tensile strength (σ_T in GPa), compressive strength (σ_C in GPa), failure strain (ε_z), and critical strain (ε_c) obtained from the mechanical tests of carbon honeycomb structures (hC28, S1, and S2).

Structure	Y	Tension		Compression	
		σ_T	ε_z	σ_C	ε_c
hC28	660	50.2	0.124	40.0	0.091
S1	597	68.7	0.157	48.1	0.086
S2	650	57.2	0.150	43.0	0.098

The S1 structure has the highest initial residual stress value (about 26.7 GPa for $\varepsilon = -0,12$), but also has the highest slope ($d\sigma/d\varepsilon = -25, 35$). In opposition, the hC28 structure has not only the lowest initial residual stress value (about 22.9 GPa for $\varepsilon = -0,12$), but also has the lowest slope ($d\sigma/d\varepsilon = -18, 77$). The S2 structure is somewhere in between S1 and hC28 regarding the initial residual stress and the slope. Since the residual stress does not drop to zero (or close to it) in any case, it means that the energy dissipated in compression is meaningful. The computed energy densities stored by each CHC under compression is the area under the tree descending plateaus, given by $E_{hC28} = 25,0 \, \mathrm{GJ\,m}^{-3}$, $E_{s1} = 30,7 \, \mathrm{GJ\,m}^{-3}$, and $E_{hC28} = 27,9 \, \mathrm{GJ\,m}^{-3}$. These values show that all CHC can dissipate energy quite well, while the S1 structure is the best one.

The representations of tensile fracture and compressive deformations are shown in **Figure 8**a–f. It can be observed that compressive loading causes local buckling of the CHC structures (Figure 8a,c,e) with exception for S1, where buckling is less localized. Tensile fracture is a process that begins with the first bond rupture in the exterior walls of the conformations from one side and quickly spreads inward until it reaches the other side. Figure 8b,d,f represents a later stage, when complete separation of the two fractured parts is completed, to observe the localization and orientation of the fracture. It is clear that in symmetrical lattices such as S1 and S2, the fracture is oriented linearly (diagonally) across the structure from the center region to one end of the structure. In the case of hC28, the fracture is not linear but irregular, mostly localized in the center region of the conformation.

Figure 9 shows the stress–strain curves for tensile and compressive loading of pure Cu and of the Cu–CHC nanocomposites. The mechanical properties extracted from these curves
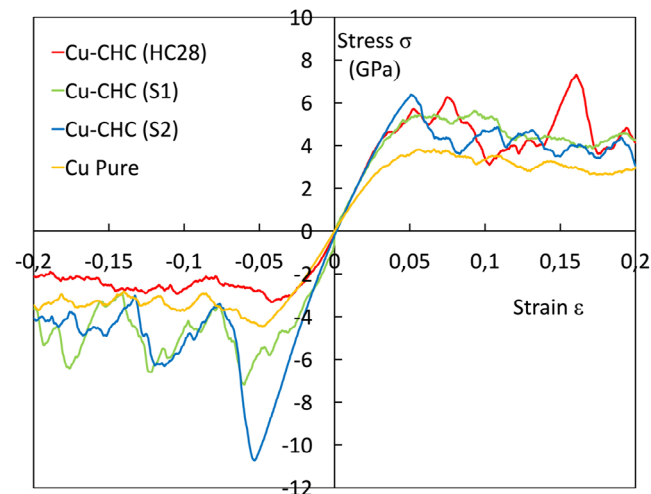

Figure 9. Stress–strain curves for compressive loading ($-0, 2 < \varepsilon < 0$) and tensile loading $0 < \varepsilon < 0, 2$) of the copper–CHC nanocomposites, namely Cu–CHC (hC28), Cu–CHC (S1), and Cu–CHC (S2).
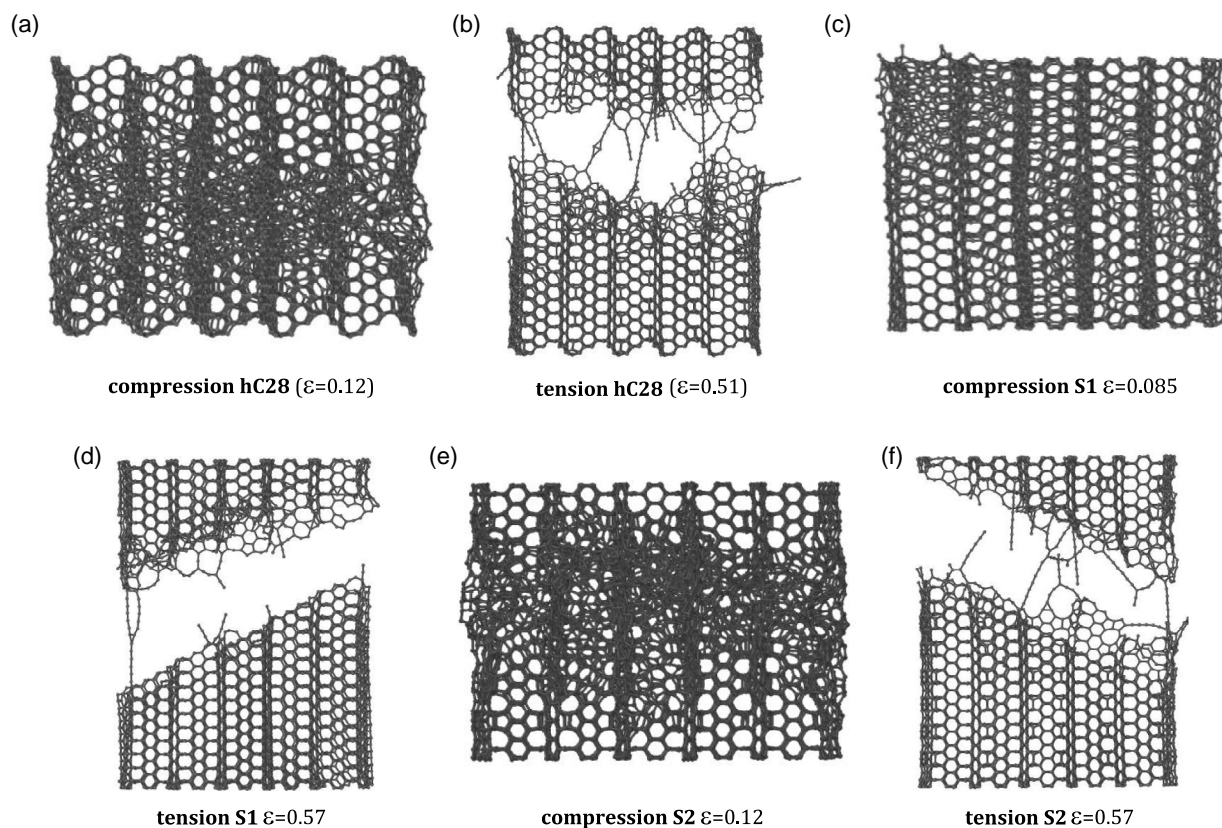

(a)

compression hC28 (ε=0.12)

(b)

tension hC28 (ε=0.51)

(c)

compression S1 ε=0.085

(d)

tension S1 ε=0.57

(e)

compression S2 ε=0.12

(f)

tension S2 ε=0.57

Figure 8. Representations of the deformed structures of CHCs under compressive loading: a) hC28, c) S1, and e) S2; and under tensile loading b) hC28, d) S1, and f) S2. Note that the respective engineering strain corresponding to the deformation is also represented in the figure.

2300147 (8 of 13)

Table 4. Young's modulus (Y in GPa), tensile strength (σ_T in GPa), compressive strength (σ_C in GPa), failure strain (ε_z), and critical strain (ε_c) obtained from the mechanical tests of pure copper and copper–carbon honeycomb nanocomposites (Cu–CHC [hC28], Cu–CHC [S1], and Cu–CHC [S2]). The variation percentage of these properties with respect to those of the recrystallized pure copper matrix is also shown.

| Structure | Y | % | Tension | | | Compression | | | | |
			σ_T	%	ε_z	%	σ_C	%	ε_c	%
Cu (recrystallized matrix)	111	–	3.82	–	0.066	–	4.45	–	0.048	–
Cu–CHC (hC28)	142	+28	5.71	+49	0.053	−20	3.32	−25	0.042	−13
Cu–CHC (S1)	165	+49	5.46	+43	0.066	0	7.18	+61	0.060	+25
Cu–CHC (S2)	167	+50	5.59	+46	0.051	−23	11.52	+159	0.053	+10

are presented in **Table 4**. The Young's modulus obtained for recrystallized Cu (111 GPa) is in good agreement with the accepted value for Cu (120 GPa—not single crystal),[45] although the purpose of recrystallizing the pure Cu matrix is for comparison purposes with the mechanical properties of the nanocomposites and not for obtaining the mechanical properties of the metal, since the quenched method used here and the size of the simulated system are not optimized for that objective.

The calculated Young's modulus of the nanocomposites clearly shows that the introduction of CHC nanofillers truly reinforce the Cu matrix. There is a gain in Y between 28% and 50% when compared to pure Cu. The tensile strength also increases around 50%, while the failure strains show small decreases. The different CHC conformations have slightly different behaviors as nanofillers reinforcement. hC28 nanofiller presents the smaller increase in Y (28%), and although other properties are in line with the other conformations, compressive strength decreases when compared to the pure metal matrix. S1 and S2 show evident increases in tensile strength and most notably in compressive strength (+159% for S2). Weaker mechanical properties from the hC28 nanofiller (inferior tensile and compressive strength when compared to other conformations, see Table 3) and a slightly inferior-recrystallization yield may be responsible for the comparatively inferior mechanical properties of Cu–CHC (hC28). Based on the results from Cu–CHC (hC28) and Cu–CHC

(S2) (S1 is a purely theoretical conformation), it can be said that CHCs nanofillers are excellent reinforcements for copper, and that regular (S2 type) CHCs are the most effective reinforcements.

Figures 10 and 12 depict the local stress distribution in the Cu–CHC nanocomposites for compressive loading at critical strains (Figure 10) and for tensile loading at rupture strains (Figure 12). The representations show a top-view perspective of 3/4 cut of the nanocomposite matrix. Negative values of stress correspond to regions under compression while positive stress values to regions under tension. In the figures, carbon atoms are represented in gray.

Both for compression and tension, there are three regions with distinct stress distributions: the bulk of the Cu matrix around the nanofiller; the interface region; and the Cu nanopillars inside the CHC tubular pores.

In the case of compression of the nanocomposites, it is clear that in the bulk, Cu atoms are under compressive stress (more pronounced in Cu–CHC [S2]), which is confirmed by the stress–strain curves in Figure 9, hence the dark blue color according to the figure legend. Major differences in stress values can be seen along grain boundaries (see Figure 10a) Cu–CHC (hC28), and Figure 10b Cu–CHC (S1) which suggests dislocations at this stage of compression may be localized in grain boundaries. Since Cu–CHC (hC28) has more grain boundaries,
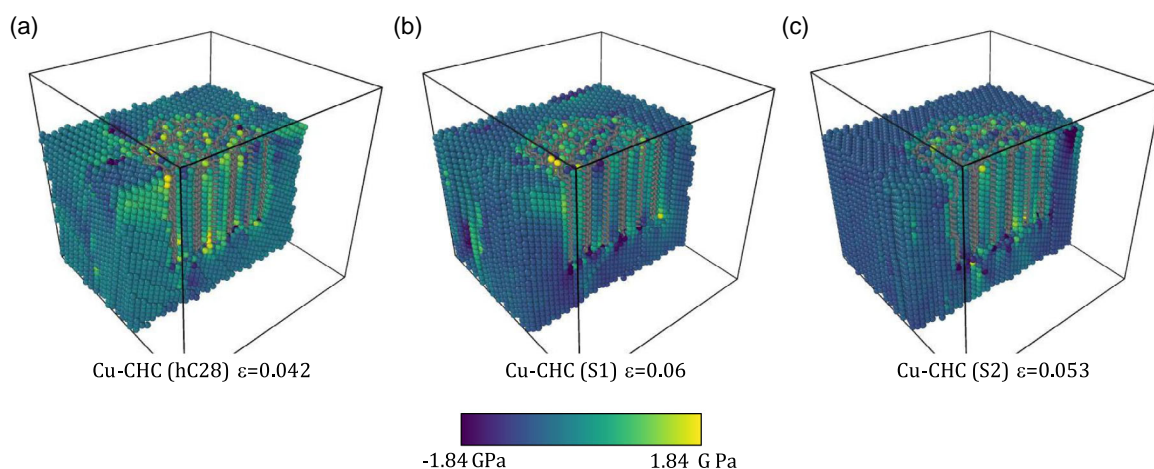

(a)   (b)   (c)

Cu-CHC (hC28) ε=0.042   Cu-CHC (S1) ε=0.06   Cu-CHC (S2) ε=0.053

-1.84 GPa   1.84 G Pa

Figure 10. Representation of stress distribution in compression loading of a) Cu–CHC (hC28), b) Cu–CHC (S1), and c) Cu–CHC (S2). Positive values indicate tensile stress and negative values denote compressive stress. The top view of ¼ of the nanocomposite was obtained by cutting the simulation box in half along xy plane and in half along the yz plane to obtain a good view of the nanofiller.

stress release is easier than for example in Cu–CHC (S2), hence less darker regions. In the interface region, Cu atoms are slightly less compressed than in the bulk region, which may indicate an improved load transfer between metal and CHC. This effect is more notable in Cu–CHC (hC28), suggesting that grain boundaries may contribute to improve load transfer between both materials. The Cu nanopillars inside the CHC benefit from the compressive load distribution to the CHC structure since they are less compressed than the bulk region.

Figure 11 represents a half cut of the simulation box (along the yz plane) to allow the observation of the nanofillers' aspect when the nanocomposites are heavily stressed. At this stage of compression ($\varepsilon = 0.38$), the nanofillers are not buckled but some of the outer honeycomb walls at the top and bottom are somewhat flattened. This is very notable for hC28 and S1 (Figure 11a, b) in particular. See Figure S2, Supporting Information, for additional insight. In general, the nanofillers are slightly tilted on their side in contrast to their positioning in the beginning of the simulations which were in alignment with z-direction. In addition, the formation of voids (regions without Cu atoms) inside the nanocomposite as a direct effect of compressive loading is also observable in one side of the CHC. The presence of the nanofiller and its angled positioning as a result of loading appear to have triggered the formation of voids in the Cu matrix. This happens regardless of the type of CHC.

In the case of tensile loading (**Figure 12**), the stress distribution in the bulk depends on the recrystallization of the Cu matrix. The effect of grain boundaries on the stress distribution is more pronounced in Cu–CHC (hC28) where tensile stress varies more slightly across regions with different orientation. In the case of Cu–CHC (S1) and Cu–CHC (S2), twinning planes clearly separate regions with different levels of tensile stress (more pronounced in Cu–CHC [S2]). The interface region has higher levels of stress than the bulk, particularly the top and bottom interface regions. Stress is also higher in the top and bottom halves of the Cu nanopillars (inside the honeycomb lattices), which may indicate that these regions (interface and nanopillars) are more prone to fracture.

Figure 13 shows a half cut of the simulation box (along the yz plane) to permit the observation of the nanofillers in a late stage of traction ($\varepsilon = 0.60$). The nanofillers roughly maintain the initial alignment with the z-direction and present no deformation in their conformation as a result of tensile loading, see Figure S3, Supporting Information. At this stage of tensile strain, the Cu matrices present a large void (absence of Cu atoms) at the top (or bottom in Cu–CHC [S1]) of the CHC which indicates previous fracture of the nanocomposite. The dimensions and form of the void are not related to the type of lattice of the CHC, but merely to the presence of the 3D nanofiller inside the Cu matrix. Fracture of the nanocomposite begins at the top or bottom of the
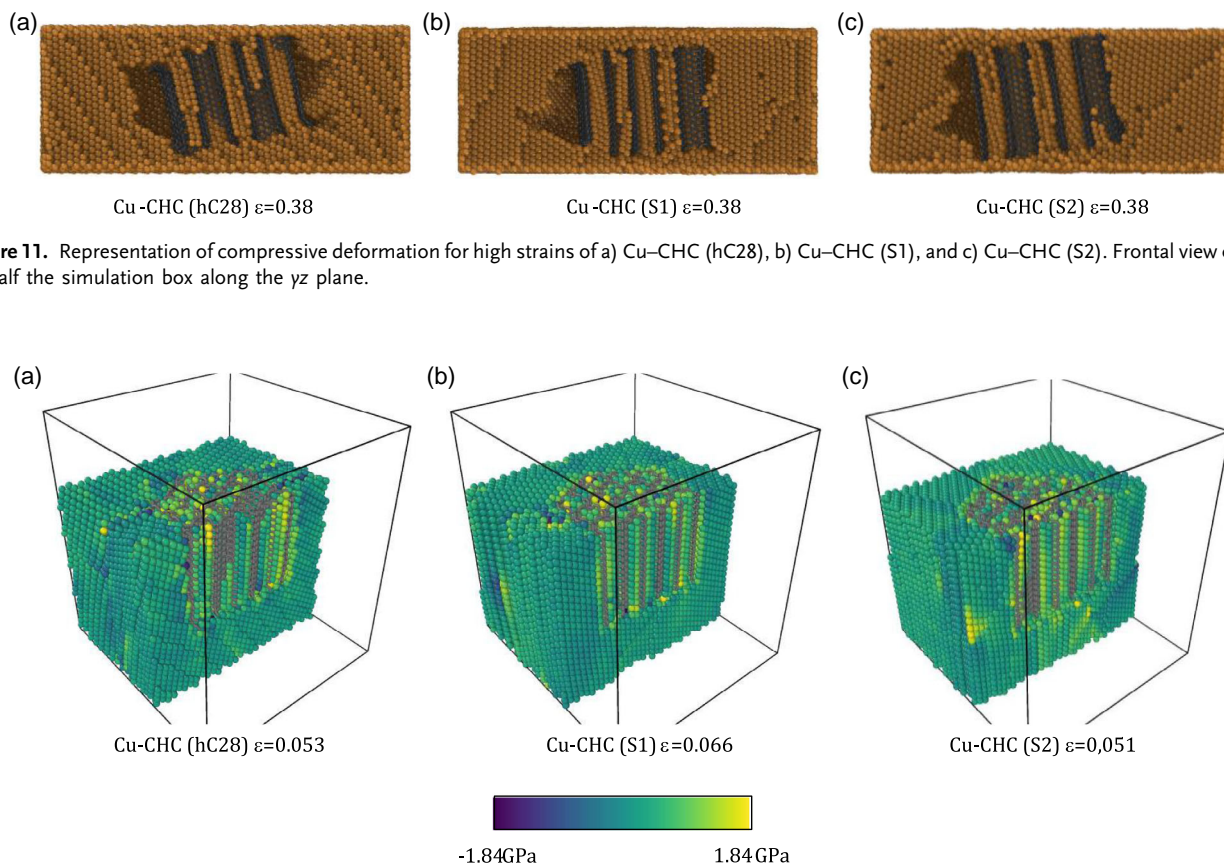

Figure 11. Representation of compressive deformation for high strains of a) Cu–CHC (hC28), b) Cu–CHC (S1), and c) Cu–CHC (S2). Frontal view of a cut of half the simulation box along the yz plane.

Figure 12. Stress distribution in tensile loading of a) Cu–CHC (hC28), b) Cu–CHC (S1), and c) Cu–CHC (S2). Positive values indicate tensile stress and negative values denote compressive stress. The top view of ¼ of the nanocomposite was obtained by cutting the simulation box in half along xy plane and in half along the yz plane to obtain a good view of the nanofiller.
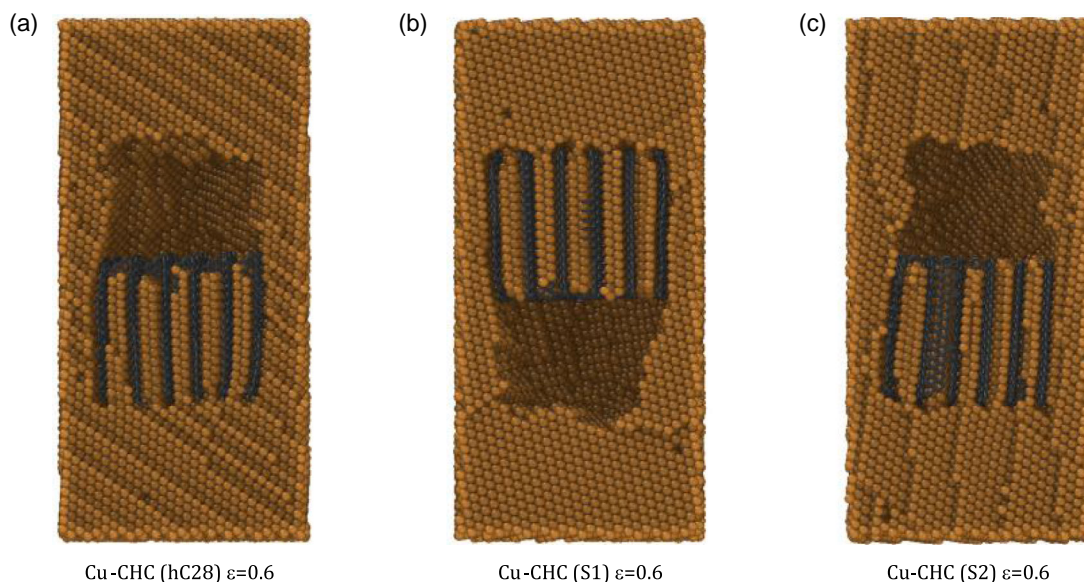
Figure 13. Representation of matrix deformation for high strains of tensile loading for a) Cu–CHC (hC28), b) Cu–CHC (S1), and c) Cu–CHC (S2). Frontal view of a cut of half the simulation box along the *yz* plane.

CHC in accordance with the previous observation that stress concentrates in these areas.

It has been already stated that reinforcement of Cu with CHCs nanofillers depends on the 1) elasticity of the nanofillers and 2) the mechanical properties of the nanocomposites. These factors were detailedly addressed in previous sections, and it was concluded that CHCs clearly reinforce the metal irrespective of the conformation of the CHC. One of the reasons for the improvement of the mechanical properties of the nanocomposites is likely the good stress transfer at the interface between the metal and the nanofiller. To unveil the improvement in adhesion between the two materials, pullout tests were conducted, and the results are presented in Section 3.3.

3.3. Pullout Behavior

In the pullout simulations, CHCs are surrounded by Cu atoms at three interfaces: 1) Cu nanopillars interacting with the inner walls of the CHC hexagonal cells; 2) Cu atoms in the bulk interacting with the outer CHC sidewalls; and 3) bulk Cu atoms interacting with Cu atoms in the nanopillars and carbon atoms at the base of the CHC (note that the "top" of the CHC is fixed and interacts only with the vacuum to where the CHC is being pulled). It should be reminded that metal–carbon interactions are nonbonded interactions modeled by LJ potential. **Figure 14**a shows the variation of force with displacement for the pullout of the three CHCs from their Cu matrices. The pullout displacement is measured as the length of CHC displaced from the initial position (L) divided by the length of the CHC (L_T); hence, for $L/L_T > 1$, the CHC is completely out of the Cu matrix. Figure 14b describes the variation of the interaction energy between metal and CHC with the pullout displacement. **Figure 15** presents some profile views of the pullout, where all Cu atoms from the bulk were deleted except those from the
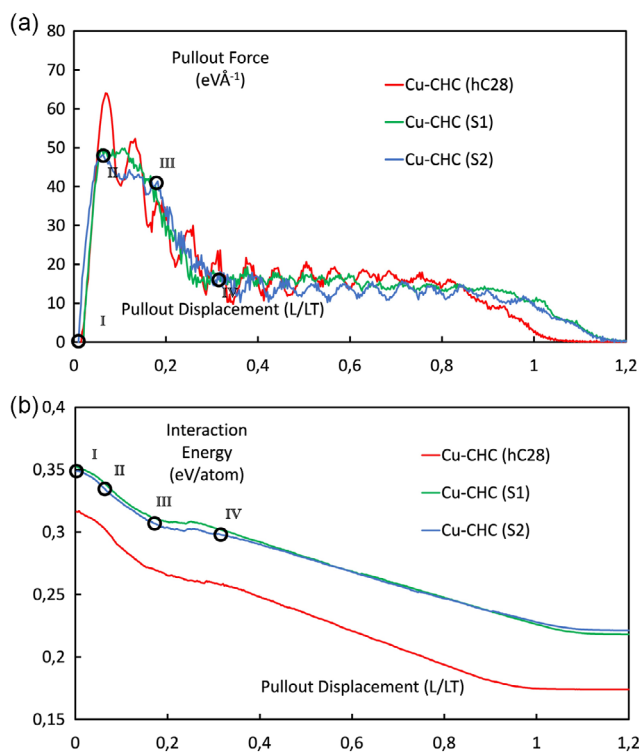

Figure 14. Variation of a) pullout force and b) interaction energy per carbon atom between the CHCs and the Cu matrix with pullout displacement (L/L_T, where L is the measured displacement from the initial position of CHC, and L_T is the length of the CHC. The black circumferences inserted in the pullout curve of Cu–CHC (S2) correspond to I − $L/L_T = 0$, II − $L/L_T = 0.06$, III − $L/L_T = 0.18$, and IV − $L/L_T = 0.32$, respectively.

interior nanopillars of the CHC and those from the base of the CHC (left side on the Figures). Hopefully, these profile cuts
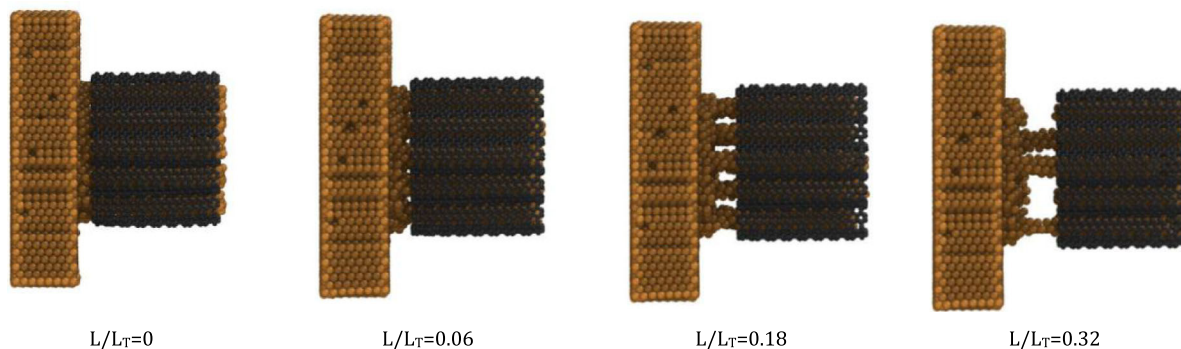
**ADVANCED
SCIENCE NEWS**

www.advancedsciencenews.com

**ADVANCED
ENGINEERING
MATERIALS**

www.aem-journal.com

| L/L$_T$=0 | L/L$_T$=0.06 | L/L$_T$=0.18 | L/L$_T$=0.32 |

Figure 15. Profile views of the pullout of the CHC (S2) from the Cu matrix. The four views correspond to pullout displacements (L/L_T) indicated by black circumferences in Figure 14. These views were obtained to highlight the detachment behavior of the Cu atoms inside the CHC; therefore, it only shows the Cu atoms belonging to the base where the CHC stands (left side), the Cu atoms inside the CHC and the CHC itself. All other Cu atoms from the Cu matrix were deleted to obtain these representations.

provide a better grasp of the pullout process. These profile views were taken at particular pullout displacements (L/L_T) which were also marked as black circumferences and respectively numbered (I–IV) on the pullout force and interaction energy curves in Figure 14a,b and that are relevant for the understanding of the pullout process.

At I, the system is equilibrated, and no pullout is imposed. In this reference state, the interaction energy is maximum since all possible Cu atoms at the interface are interacting with C atoms from the CHC. Phase II is the peak of the pullout force curve. Until this point, Cu nanopillars have been dragged from the Cu base bulk due to their strong interaction with the CHC inner walls (which are being pulled) and as these metal–metal and metal–carbon interactions are stretched force increases. At II, the Cu nanopillars begin to "detach" from the CHC and slide away but continue to have a strong interaction with CHC; therefore, the pullout force decreases only slightly between II and III. In contrast, between I and II, as carbon atoms distance themselves from the base composed of Cu atoms, interaction energy begins to slightly decrease. This decrease becomes more evident (steep slope in interaction energy curve) as the nanopillars begin to slide inside the CHC (between II and III), because those carbon atoms from the top of the CHC start to lose interaction with Cu atoms as they are being pulled out of the Cu matrix. Between III and IV, most of the Cu nanopillars (not all) break from the Cu base, which significantly lowers the pulling force. Whenever the Cu nanopillars are maintained inside the CHC, the interaction energy does not decrease appreciably.

From phase IV to the end of the pullout process, the force remains constant since only sliding occurs: the three Cu nanopillars attached to the Cu base are sliding away inside the CHC and the CHCs with the detached Cu nanopillars are sliding off the Cu matrix. The interaction energy of phase IV onward is steadily decreasing because the interface between the outer walls of CHC and bulk Cu is shrinking as the CHC is pulled off the Cu matrix. At $L/L_T = 1$, the CHC is out of the Cu matrix, the force is null, and the interaction energy is constant because it refers to the interaction between the Cu nanopillars and the CHC carbon atoms. These observations are valid for all three nanocomposites since the pullout behavior, as can be seen from Figure 14, is similar between them. Figure 15 presents profile views from I to IV for Cu–CHC (S2). For profile views of phases I–IV of Cu–CHC (hC28) and Cu–CHC (S1), the reader is referred to Figure S4, Supporting Information.

The fact that most Cu nanopillars remained inside the CHC during the pullout, detaching themselves from the Cu base gives a clear indicator that adhesion between a Cu matrix and the CHC is strong. To this fact contributes the 3D conformation of the CHCs and the tubular honeycomb cells that can be filled with Cu atoms, which greatly increase the interaction interface between the two materials. In this case, it can also be observed that the CHC lattice type has little influence on the pullout behavior of the CHC, with exception to hC28 which has a higher pullout force.

4. Conclusions

The mechanical reinforcement of copper with 3D graphene networks, namely CHCs, was studied using MD simulations. The interface metal–carbon was accurately modeled by melting and recrystallizing the Cu matrix around the nanofiller, which allowed the Cu atoms to penetrate and disperse into the tubular honeycomb cells of the porous CHC, forming Cu nanopillars upon cooling. It was found that the 3D conformation of CHCs avoids the formation of large FCC crystals, lowering somewhat the recrystallization yield. The presence of the nanofillers also increased the phase-transition temperature of Cu in the nanocomposites.

Tensile and compressive loading were imposed on the nanocomposites in the direction of the CHC cell axis by deforming the simulation box. An increase of the Young's modulus of the nanocomposites was found between 28% and 50%. Tensile strength showed increases between 43% and 49%, while compressive strength reached gains as high as 159%. Rupture strains mostly decreased in comparison to pure Cu, while critical strains generally showed small increases.

Pullout tests were also performed to assess the level of adhesion between nanofiller and metal matrix. It was unveiled that the copper nanopillars formed inside the CHC are responsible by a notable increase in pullout force, because these structures significantly enlarge the interface surface between the two materials, thus increasing the interaction energy. It was also predicted that these nanopillars detach from the Cu matrix, remaining inside the CHC when the latter is pulled out of the matrix. Overall, CHCs are superior alternatives to graphene in the mechanical reinforcement of copper and predictably of metals.

Supporting Information

Supporting Information is available from the Wiley Online Library or from the author.

Conflict of Interest

The authors declare no conflict of interest.

Data Availability Statement

The data that support the findings of this study are available from the corresponding author upon reasonable request.

[1] A. Saboori, M. Dadkhah, P. Fino, M. Pavese, *Metals* **2018**, *8*, 423.
[2] S. Zhao, Y. Zhang, J. Yang, S. Kitipornchai, *J. Mater. Sci. Technol.* **2022**, *120*, 196.
[3] D. Janas, B. Liszka, *Mater. Chem. Front.* **2018**, *2*, 22.
[4] F. Scarpa, S. Adhikari, A. J. Gil, C. Remillat, *Nanotechnology* **2010**, *21*, 125702.
[5] S. Deng, V. Berry, *Mater. Today* **2016**, *19*, 197.
[6] C. Li, G. Shi, *Nanoscale* **2012**, *4*, 5549.
[7] H. R. Karfunkel, T. Dressier, *J. Am. Chem. Soc.* **1992**, *114*, 2285.
[8] N. v. Krainyukova, E. N. Zubarev, *Phys. Rev. Lett.* **2016**, *116*, 055501.
[9] N. v. Krainyukova, *J. Low Temp. Phys* **2017**, *187*, 90.
[10] N. v. Krainyukova, B. Kuchta, L. Firlej, P. Pfeifer, *Low Temp. Phys.* **2020**, *46*, 219.
[11] W. Zhou, H. Xie, S. Wang, Q. Wang, P. Jena, *Carbon N Y* **2020**, *168*, 163.
[12] Y. Gao, Y. Chen, C. Zhong, Z. Zhang, Y. Xie, S. Zhang, *Nanoscale* **2016**, *8*, 12863.
[13] Q. Qin, X. Liu, H. Wang, T. Sun, F. Chu, L. Xie, P. Brault, Q. Peng, *Nanotechnology* **2021**, *32*, 375705.
[14] Y. Du, J. Zhou, P. Ying, J. Zhang, *Comput. Mater. Sci.* **2021**, *187*, 110125.
[15] J. Zhang, *Carbon N Y* **2018**, *131*, 127.
[16] H. Zhang, S. Hu, H. Wang, Y. Chen, H. Wang, Y. Ni, *Chin. J. Phys.* **2019**, *59*, 567.
[17] Z. Yang, G. Lan, B. Ouyang, L.-C. Xu, R. Liu, X. Liu, J. Song, *Mater. Chem. Phys.* **2016**, *183*, 6.
[18] L. Yi, T. Chang, X. Q. Feng, Y. Zhang, J. Wang, B. Huang, *Carbon N Y* **2017**, *118*, 348.
[19] Z. Pang, X. Gu, Y. Wei, R. Yang, M. S. Dresselhaus, *Nano Lett.* **2017**, *17*, 179.
[20] Z. Zhang, A. Kutana, Y. Yang, N. v. Krainyukova, E. S. Penev, B. I. Yakobson, *Carbon N Y* **2017**, *113*, 26.
[21] X. Gu, Z. Pang, Y. Wei, R. Yang, *Carbon N Y* **2017**, *119*, 278.
[22] Q. Qin, H. An, C. He, L. Xie, Q. Peng, *Nanotechnology* **2019**, *30*, 325704.
[23] L. Cao, F. Fan, *Extreme Mech. Lett.* **2020**, *39*, 100861.
[24] S. Zhang, Y. Zhu, F. Wang, X. Liu, H. Wu, S. N. Luo, *Compos. B Eng.* **2021**, *219*, 108967.
[25] J. Zhang, C. Wang, *J. Phys. Chem. C* **2017**, *121*, 8196.
[26] Y. Zhang, Q. An, J. Li, B. Lu, W. Wu, R. Xia, *J. Mol. Model.* **2020**, *26*, 335.
[27] K. Chu, F. Wang, Y. B. Li, X.-H. Wang, D. J. Huang, H. Zhang, *Carbon N Y* **2018**, *133*, 127.
[28] J. Hu, W. Wu, C. Zhong, N. Liu, C. Ouyang, H. Y. Yang, S. A. Yang, *Carbon N Y* **2019**, *141*, 417.
[29] S. J. Stuart, A. B. Tutein, J. A. Harrison, *J. Chem. Phys.* **2000**, *112*, 6472.
[30] B. Faria, N. Silvestre, J. N. C. Lopes, *Comput. Mater. Sci.* **2020**, *171*, 109233.
[31] O. A. Shenderova, D. W. Brenner, A. Omeltchenko, X. Su, L. H. Yang, *Phys. Rev. B* **2000**, *61*, 3877.
[32] M. I. Mendelev, A. H. King, *Philos. Mag.* **2013**, *93*, 1268.
[33] A. Kutana, K. P. Giapis, *Phys. Rev. Lett.* **2006**, *97*, 245501.
[34] J. W. Kang, Q. Jiang, H. J. Hwang, *Nanotechnology* **2006**, *17*, 5485.
[35] A. P. Thompson, H. M. Aktulga, R. Berger, D. S. Bolintineanu, W. M. Brown, P. S. Crozier, P. J. in 't Veld, A. Kohlmeyer, S. G. Moore, T. D. Nguyen, R. Shan, M. J. Stevens, J. Tranchida, C. Trott, S. J. Plimpton, *Comput. Phys. Commun.* **2022**, *271*, 108171.
[36] B. Faria, C. Guarda, N. Silvestre, J. N. C. Lopes, *Comput. Mater. Sci.* **2020**, *176*, 109538.
[37] C. Guarda, B. Faria, N. Silvestre, J. N. C. Lopes, N. M. Pugno, *Compos. Struct.* **2022**, *292*, 115679.
[38] A. Stukowski, *Modell. Simul. Mater. Sci. Eng.* **2012**, *20*, 045021.
[39] J. D. Honeycutt, H. C. Andersen, *J. Phys. Chem.* **1987**, *91*, 4950.
[40] L. Yang, Z. Ma, A. Stukowski, *Modell. Simul. Mater. Sci. Eng.* **2009**, *18*, 015012.
[41] J. Hu, J. Zhou, A. Zhang, L. Yi, J. Wang, *Phys. Lett. A* **2021**, *391*, 127130.
[42] L. K. Rysaeva, A. I. Klyavlina, K. F. Galiachmetov, J. A. Baimova, D. S. Lisovenko, V. A. Gorodtsov, *IOP Conf. Ser. Mater. Sci. Eng.* **2018**, *447*, 012035.
[43] L. Xie, H. An, C. He, Q. Qin, Q. Peng, *Nanomaterials* **2019**, *9*, 156.
[44] H. Wang, Q. Cao, Q. Peng, S. Liu, *Nanomaterials* **2019**, *9*, 109.
[45] A. Basavalingappa, M. Y. Shen, J. R. Lloyd, *Mech. Adv. Mater. Mod. Processes* **2017**, *3*, 6.